Proceedings of the 9ICEG
9th International Congress on Environmental Geotechnics
25-28 June, 2023 | Chania, Greece
© Authors: All rights reserved, 2023
https://doi.org/10.53243/ICEG2023-446

Thermo-mechanical responses of containment materials for geoenvironmental applications

Dazhao Lu[1], and Wei Wu[2]

[1]*PhD student, Nanyang Technological University, Singapore, email: dazhao.lu@ntu.edu.sg*

[2]*Associate Professor, Nanyang Technological University, Singapore, email: wu.wei@ntu.edu.sg*

ABSTRACT

Underground space is a safe and reliable option for large-scale, cryogenic energy storage in industrial and commercial areas. In the design and operation of underground storage facilities, the performance of the storage facilities relies heavily on the thermo-mechanical responses of containment materials under external geological environments and internal storage conditions. However, the thermo-mechanical responses of containment materials under temperature gradient and earth pressure conditions remain not fully understood. Here we experimentally investigate the contributions of thermal and mechanical loads to the strain evolution of rock and concrete and highlight the influence of circular hole and rough fracture on the strain evolution. The results show that the mechanical load mainly controls the strain evolution of the intact limestone, while the thermal load strongly affects the strain evolution around the circular hole. The failure pattern of concrete primarily influences the mechanically induced strain, and the thermally induced strain is insensitive to the concrete failure. The test system can be modified and upgraded to study various research topics related to underground energy storage.

Keywords: Thermo-mechanical responses, containment materials, underground storage facilities.

1 INTRODUCTION

Energy storage plays an essential role in carbon neutrality, particularly for densely populated cities. Large-scale, cryogenic storage tanks are built conventionally aboveground for storage of liquid energy, such as liquified natural gas (LNG), but located remotely from urban areas due to safety and regulatory considerations. Underground space is a safe and reliable option for energy storage in industrial and commercial areas, and large-scale underground storage can promote the balance between energy supply and demand as well as the convergence towards a low carbon economy (Matos et al., 2019). The performance of large-scale, cryogenic storage caverns relies heavily on the thermo-mechanical responses of containment materials (e.g., concrete and geomaterials) under external geological environments and internal storage conditions. For instance, the mechanical behaviors of concrete walls at cryogenic temperatures are critical to the safe design of aboveground LNG storage tanks (Fulford and Slatter, 1988). For underground LNG storage caverns, the thickness of concrete linings can be reduced due to the confinement of earth materials. However, the lining thickness is not well addressed by the design regulations and dependent on the thermo-mechanical responses of containment materials (Rutqvist et al., 2012; Semprich et al., 1990).

Numerous studies have shown the importance of the thermo-mechanical responses of containment materials in the design and operation of underground storage facilities. A pilot study in Korea reveals that the leakage of liquid and gas through tensile cracks due to the shrinkage of containment materials is an important factor influencing the success of underground LNG storage (Park et al., 2010). The induced cracks may cause other hydraulic, thermal, and mechanical problems to underground storage caverns (Jung et al., 2011; Wanniarachchi and Wu, 2021). The cracking process should be examined closely during the first cooling cycle as indicated by acoustic monitoring during the natural gas storage in salt caverns (Balland et al., 2018). The subsequent de-pressurization and re-pressurization processes mainly affect the long-term stability of underground gas storage caverns, whereas the long-term thermal effect is likely minor (Mohanty and Vandergrift, 2012). The cooling and pressurization processes impose the thermal and mechanical loads on the surrounding materials, and most of the previous studies focus on the coupled effect on the material behaviors based on numerical simulations (Glamheden and

Lindblom, 2002; Lannaccone et al., 2021; Wang and Wu, 2022). However, understanding the individual contributions of thermal and mechanical loads to the deformation of containment materials is critical to find out the reasons behind unexpected failure of these materials and to mitigate potential risks related to the leakage of liquid and gas.

This study reports the thermo-mechanical responses of containment materials under simulated temperature gradient and earth pressure conditions. A temperature gradient test system is first described, followed by two applications using underground LNG storage as a background (e.g., the thermal and mechanical responses of rock and concrete). Future developments of the test system are also present to further solve the technical challenges related to underground energy storage.

2 EXPERIMENTAL METHOD

The temperature gradient test system applies coupled thermal and mechanical loads on a large-scale cuboid specimen to simulate temperature gradient and earth pressure on the containment materials of an underground storage facility. The specimen can be made of a single material or composed of multiple materials (e.g., steel, concrete, soil, and rock). Defects (e.g., hole and fracture) can also be prefabricated in the specimen. The deformation and failure characteristics of these materials and their interfaces under the coupled loads are monitored by various diagnostic methods (e.g., strain gauge, thermocouple, and high-speed camera) to evaluate the performance of containment materials and the safety of storage facilities.

In the test system, a test chamber hosts the cuboid specimen with the maximum allowable size of 500 (length) x 400 (height) x 400 (width) mm and provides the loading environment with an earth pressure simulator and a set of hot and cold plates (Figure 1). The axial load supplied by the earth pressure simulator with a hydraulic jack is up to 100 kN. The temperature gradient is established by the hot plate with the maximum temperature of +50 ºC and the cold plate with the minimal temperature of -190 ºC, which are sufficient to simulate the ambient temperature (+35 ºC) and the LNG temperature (-162 ºC), respectively. The temperatures on the hot and cold plates are maintained by electric heating and liquified nitrogen, respectively, and controlled by a closed-loop control software with a fluctuation of less than 1 ºC at a target temperature.

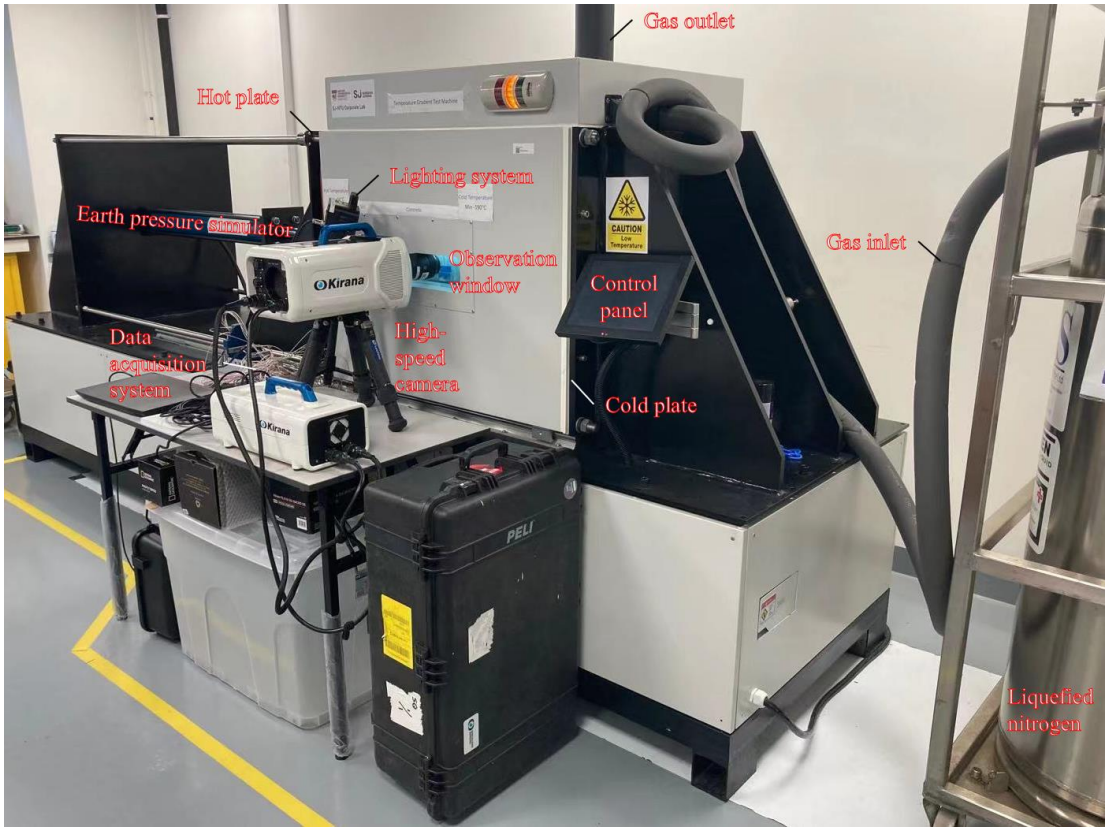


Figure 1. *Laboratory setup of temperature gradient test system.*

A LabVIEW-based data acquisition system includes a strain gauge datalogger, a temperature datalogger, and a digital module for trigger. The temperature gradient over the specimen is monitored by up to 8 thermocouples, with a sampling rate of up to 95 Hz, installed along the coupled loading direction. The deformation and failure characteristics of the specimen are either recorded locally by up to 8 strain gauges or observed globally by high-speed imaging. The strain gauges, with a sampling rate of up to 10 kHz, record local-scale deformation and pre-designed failure of containment materials. The high-speed photography observes full-scale deformation and random failure on the specimen surface via an observation window with a dimension of 500 (length) x 100 (height) mm. A Kirana high-speed camera with a focal length lens of 105 mm can be triggered either manually or automatically and has a frame rate up to 106 frames per second. Heating and lighting are supplied on the observation window to avoid frost and ensure image quality. The specimen surface next to the observation window is painted in white color and coated with black speckles for digital image correlation (DIC) analysis (Figure 2). The evolution of strain field in the region of interest is derived by tracking the coordinates and deformation of subsets on the reference and deformed images captured by the high-speed camera (Chu et al., 1985; Wang et al., 2022).

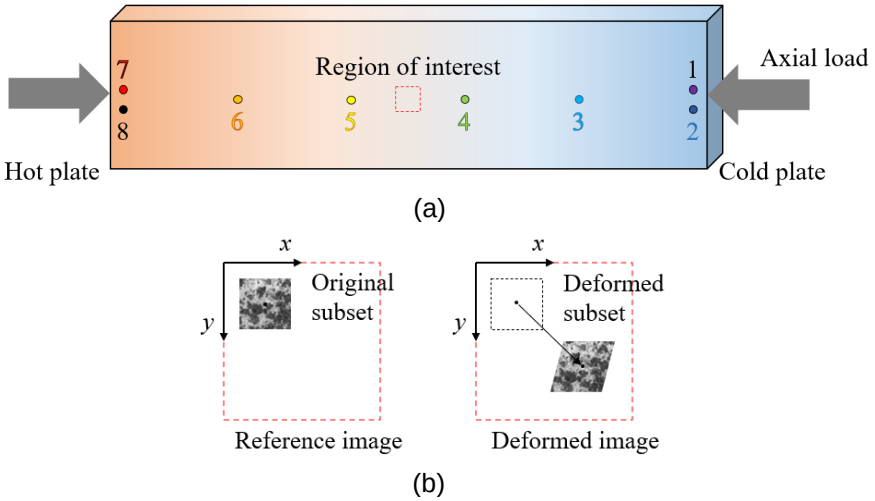


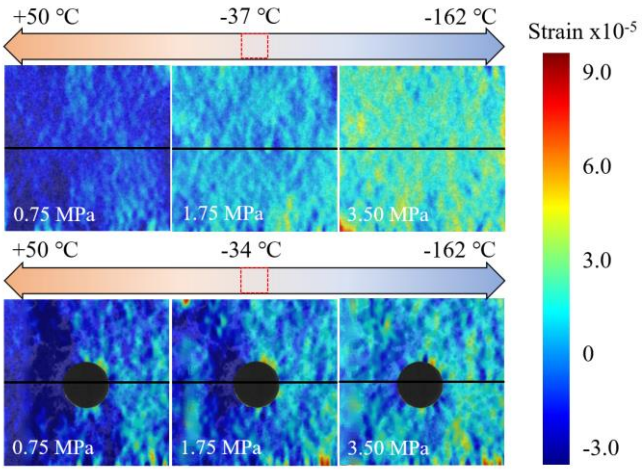
Figure 2. *(a) Distribution of thermocouples on polypropylene specimen and location of the region of interest and (b) application of digital image correlation in the region of interest.*

This study investigates the thermo-mechanical responses of intact and flawed limestone (test 1) as well as intact and fractured concrete (test 2). The initial temperature of the specimen is 20 ºC. The first test sheds light on the influence of circular flaw on the strain field of a limestone specimen, considering the variations of horizontal strain due to the thermal and mechanical loads at a temperature gradient of +50 – -162 °C and under 3 axial stresses (0.75, 1.75, and 3.50 MPa). The limestone has a bulk density of 2160 kg/m^3 and a Young's modulus of 22.5 GPa. The specimen is 500 mm in length, 100 mm in height, and 80 mm in thickness. A circular hole with a diameter of 6 mm is drilled at the center of the region of interest. The region of interest with a dimension of 20 x 20 mm is located behind the central area of the observation window and monitored by the Kirana camera. The same temperature gradients and the same axial stresses are used for comparison with the strain field over an intact limestone specimen. The second test addresses how the strain field evolves over an irregular fracture of concrete specimen with a dimension of 500 (length) x 200 (height) x 80 (thickness) mm under the thermal and mechanical loads. The C40 concrete has a bulk density of 2300 kg/m^3 and a Young's modulus of 28.0 GPa. The fracture is obtained by axial splitting with a root mean square roughness of 0.1 mm. The temperature gradient is +30 – -120 °C, and the axial stresses are 0.50, 1.50, and 2.00 MPa. The strain field over an intact concrete specimen is also shown for comparison.

3 RESULTS AND DISCUSSION

In the first test, the horizontal strain of intact limestone specimen changes from negative under 0.75 MPa axial stress to positive under 3.50 MPa axial stress (Figure 3a). The variations of horizontal strain due to the thermal and mechanical loads can be explained based on the mechanically induced strain and the thermally induced strain along the central line of the region of interest. The total horizontal strain along the central line is computed using the image at 0 temperature gradient and under 0 axial stress

as the reference for the DIC analysis. The mechanically induced strain is obtained by subtracting the total horizontal strain under a low axial stress from that under a high axial stress while keeping the same temperature in the region of interest. Similarly, the thermally induced strain is calculated by subtracting the total horizontal strain at a low temperature gradient from that at a high temperature gradient while keeping the same axial stress. The mechanically induced strain and the thermally induced strain can be calculated individually because the thermo-mechanical coupling effect is negligible due to the product of linear thermal expansion coefficient and initial temperature is far less than 1/3 (Barron and Barron, 2012). The total horizontal strain is equal to the mechanically induced strain plus the thermally induced strain at a given temperature gradient under the same axial stress. Figure 3b reveals that the mechanically induced strain increases with a higher axial stress while the thermally induced strain has negligible changes. The mechanically induced strain approaches 0 under 0.75 MPa axial stress and the thermally induced strain is negative at a temperature of -37 °C, so the total horizontal strain is negative. Under 1.75 MPa axial stress, the mechanically induced strain is comparable to the thermally induced strain, and the total horizontal strain thus fluctuates around 0. For 3.50 MPa axial stress, the total horizontal strain is positive as the mechanically induced strain is much larger than the thermally induced strain. Figure 3b indicate that the mechanical load mainly contributes to the strain evolution of the intact limestone specimen. Additionally, the thermally induced strain due to a sub-zero temperature may not result in material contraction, depending on the relative value of mechanically induced strain. As shown in Figure 3c, the DIC results show that the existence of central hole remarkably modifies the distribution of horizontal strain with negative strain on the side with a high temperature in both the cases. The horizontal strain on the other side is negative at a temperature of -34 °C. The total horizontal strain is also decomposed into the mechanically induced strain and the thermally induced strain to explain the strain distribution. Along the central line, the mechanically induced strain is roughly symmetrical on both sides of the central hole, similar to the previous DIC analysis (Li et al., 2017), and fluctuates around a small strain value due to a minor change in axial stress relative to the Young's modulus of the limestone (22.5 GPa). The thermally induced strain thus plays a vital role in controlling the total horizontal strain. Unlike the mechanically induced strain, the thermally induced strain exhibits a complex distribution with negative strain on the side with a high temperature (left side) and positive strain on the other side (right side).



(a)

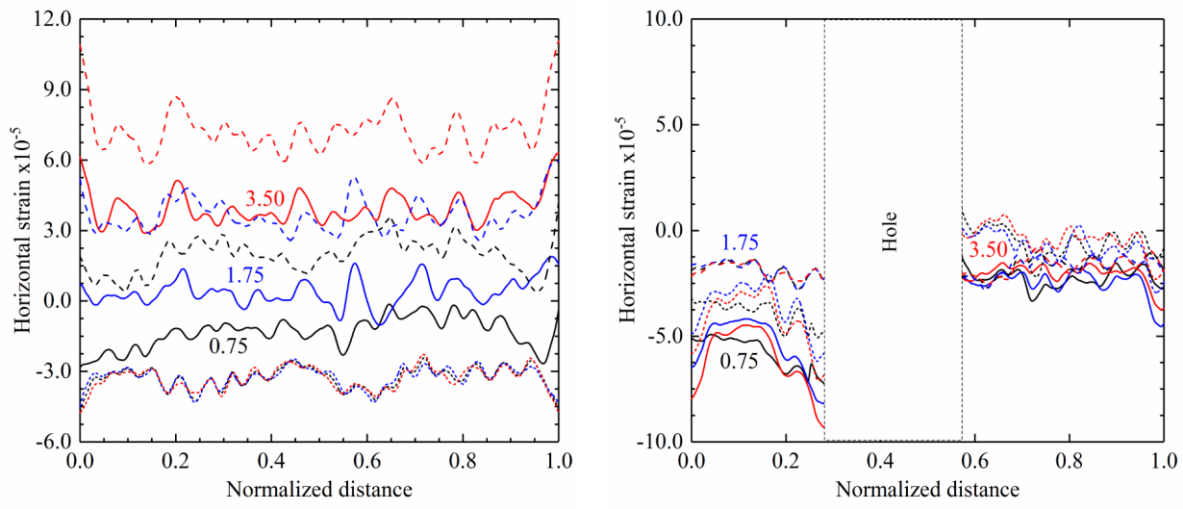
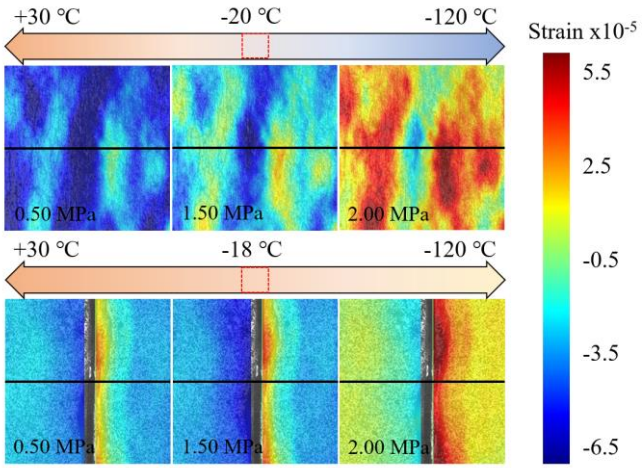
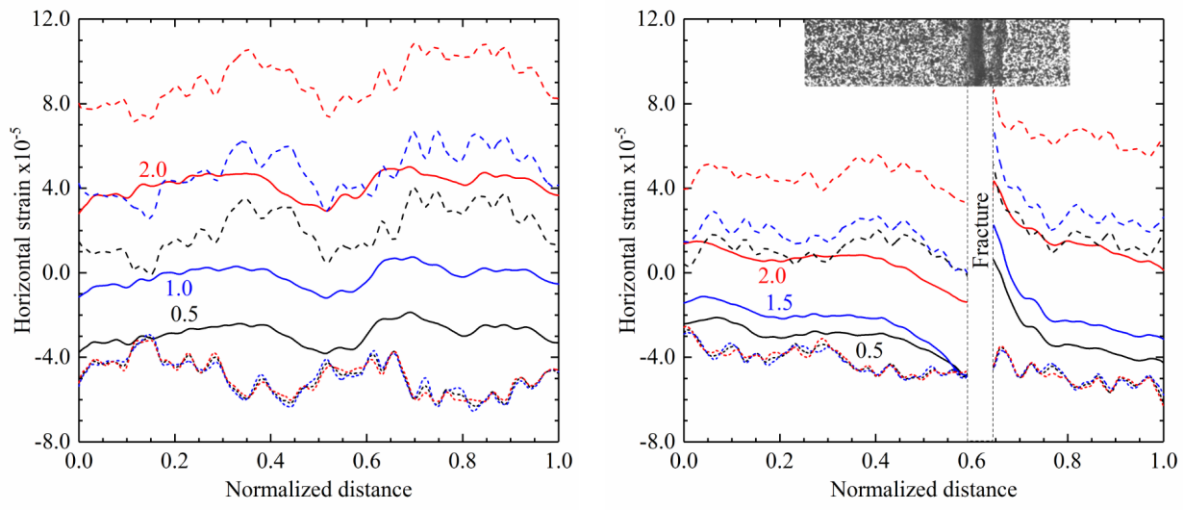


Figure 3. *Strain evolution of intact limestone (upper) and flawed limestone (lower) at the same temperature gradient (+50 – -162 °C) under coupled thermo-mechanical loads, (a) horizontal strain in the region of interest (red box) derived by DIC analysis, the color arrow highlights temperature variation from the hot plate (left) to the region of interest (middle) and to the cold plate (right), and the black line indicates the central line of the region of interest, (b) total horizontal strain (solid line), mechanically induced strain (dashed line), and thermally induced strain (dotted line) along the central line on the intact concrete, (c) total horizontal strain (solid line), mechanically induced strain (dashed line), and thermally induced strain (dotted line) along the central line on the fractured concrete. The inset image exhibits defect on the left side of the fracture, resulting in lower horizontal strain than the right side.*

For the second test on intact and fracture concrete specimens, the temperatures in the region of interest are around -20 and -18 °C, respectively. The DIC results exhibit that the concrete material is more heterogenous than the limestone material, particularly under higher axial stresses, and the fracture fully modifies the distribution of strain field (Figure 4a). After decomposing the total horizontal strain, the mechanically induced strain of the intact specimen grows with an increase in axial stress, and the thermally induced strain shows minor changes (Figure 4b). The fracture has a negligible influence on the thermally induced strain, but the failure pattern significantly affects the mechanically induced strain on two sides of the fracture. Figure 4c depicts that the mechanically induced strain on the left side of the fracture is much lower than that on the right side. The inset photo illustrates that a secondary crack parallel to the fracture likely promotes the deformation on the right side. This observation highlights that the complexity of strain field on the fractured concrete dominated by the failure pattern of the concrete specimen.



(a)



(b) (c)

Figure 4. *Strain evolution of intact concrete (upper) and fractured concrete (lower) at the same temperature gradient (+30 – -120 °C) under coupled thermo-mechanical loads, (a) horizontal strain in the region of interest (red box) derived by DIC analysis, the color arrow highlights temperature variation from the hot plate (left) to the region of interest (middle) and to the cold plate (right), and the black line indicates the central line of the region of interest, (b) total horizontal strain (solid line), mechanically induced strain (dashed line), and thermally induced strain (dotted line) along the central line on the intact concrete, (c) total horizontal strain (solid line), mechanically induced strain (dashed line), and thermally induced strain (dotted line) along the central line on the fractured concrete. The inset image exhibits defect on the left side of the fracture, resulting in lower horizontal strain than the right side.*

In this study, we demonstrate the typical applications of the temperature gradient test system to investigate the thermo-mechanical responses of intact, flawed, and fractured containment materials. The DIC analysis quantifies the individual contributions of thermal and mechanical loads to the deformation of containment materials, which is important to forecast potential failure of these materials in underground storage facilities. The test system can be extended to study other topics related to underground energy storage. For instance, the dynamic responses of containment materials under loading and unloading conditions, which can take full advantage of high-speed photogrammetry. The groundwater condition can be simulated by building a water tank in the test chamber and immersing the specimen in the water tank. The internal pressure associated with the storage of liquid and gas can also be mimicked by inserting a liquid-filled expandable capsule in the central hole and controlled by a hydraulic pump.

4 CONCLUSIONS

We experimentally investigate the thermo-mechanical responses of containment materials under simulated temperature gradient and earth pressure conditions and demonstrated the individual contributions of thermal and mechanical loads to the strain evolution of flawed rock and fractured concrete. Our results show that the thermally induced strain due to a sub-zero temperature may not result in material contraction, depending on the relative value of mechanically induced strain. The results also show that the existence of flaw and fracture can remarkably modify the distribution of strain under thermal and mechanical loads. Our study is important to forecast potential failure of containment materials and to eventually optimize the design and operation of underground storage facilities. A future study will improve the test system to further solve the technical challenges related to underground energy storage.

REFERENCES

Balland, C., Billiotte, J., Tessier, B., Raingeard, A., Hertz, E., Hévin, G., Tribout, D., Thelier, N., Hadj-Hassen, F., Charnavel, Y., Bigarré, P. (2018). Acoustic monitoring of a thermo-mechanical test simulating withdrawal in a gas storage salt cavern. Int. J. Rock Mech. Min. Sci. 111, 21-32.

Barron, R.F., Barron, B.R. (2012). Design for thermal stresses. John Wiley & Sons, Inc.

Chu, T.C., Ranson, W.F., Sutton, M.A., Peter, W.H. (1985). Applications of digital-image-correlation techniques to experimental mechanics. Exper. Mech. 25 (3), 232-244,

Fang, Z., Wu, W. (2022). Laboratory friction-permeability response of rock fractures: a review and new insights. Geomech. Geophys. Geo-energ. Geo-resour. 8 (1), 15.

Fulford, N.J., Slatter, M.D. (1988). Developments in the safe design of LNG tanks. Cryogenics 28 (12), 810-817.

Glamheden, R., Lindblom, U. (2002). Thermal and mechanical behavior of refrigerated caverns in hard rock. Tunnel. Undergr. Space Technol. 17 (4), 341-353.

Lannaccone, T., Scarponi, G.E., Landucci, G., Cozzani, V. (2021). Numerical simulation of LNG tanks exposed to fire. Process Safety Environ. Protect. 149, 735-749.

Li, D., Zhu, Q., Zhou, Z., Li, X., Ranjith, P.G. (2017). Fracture analysis of marble specimens with a hole under uniaxial compression by digital image correlations. Eng. Frac. Mech. 183, 109-124.

Li, Z., Ma, X., Kong, X.Z., Saar, M.O., Vogler, D. (2023). Permeability evolution during pressure-controlled shear slip in saw-cut and natural granite fractures. Rock Mech. Bull. 2, 10027.

Jung, Y.B., Park, E.S., Chung, S.K., Kim, H.Y. (2011). Coupled hydro-thermal modeling of ice ring formation around a pilot LNG cavern in rock. Eng. Geol. 118 (3-4), 122-133.

Matos, C.R., Carneiro, J.F., Silva, P.P. (2019). Overview of large-scale underground energy storage technologies for integration of renewable energies and criteria for reservoir identification. J. Energy Storage 21, 241-258.

Mohanty, S., Vandergrift, T. (2012). Long term stability evaluation of an old underground gas storage cavern using unique numerical methods. Tunnel. Undergr. Space Technol. 30 (4), 145-154.

Park, E.S., Jung, Y.B., Song, W.K., Lee, D.H., Chung, S,K. (2010). Pilot study on the underground lined rock cavern for LNG storage. Eng. Geol. 116 (1-2), 44-52.

Rutqvist, J., Kim, H.M., Ryu, D.W., Synn, J.H., Song, W.K. (2012). Modeling of coupled thermodynamic and geomechanical performance of underground compressed air energy storage in lined rock caverns. Int. J. Rock Mech. Min. Sci. 52, 71-81.

Semprich, S., Crotogino, F., Schneider, H.J. (1990). Storage in lined hard-rock caverns: results of a pilot study. Tunnel. Undergr. Space Technol. 5 (4), 309-313.

Shirole, D., Walton, G., Hedayat, A. (2020). Experimental investigation of multi-scale strain-field heterogeneity in rocks. Int. J. Rock Mech. Min. Sci. 127, 104212.

Wang, L., Wei, M., Wu, W. (2022). Control of dynamic failure of brittle rock using expansive mortar. Acta Geotech. 17 (12), 5829-5839.

Wang, L., Wu, W. (2022). Modelling of dynamic tensile failure of inclusion-bearing rocks. Geomech. Geophys. Geo-energ. Geo-resour. 8 (5), 168.

Wanniarachchi, W.A.M., Wu, W. (2021). Permeability evolution of rock-concrete interfaces in underground lined storage systems. Int. J. Rock Mech. Min. Sci. 143, 104792.

Yamabe, T., Neaupane, K.M. (2001). Determination of some thermo-mechanical properties of Sirahama sandstone under subzero temperature condition. Int. J. Rock Mech. Min. Sci. 38 (7), 1029-1034.